

Some Experimental Tools

Pressure response of Strongly Correlated Electron Systems

by *E. Bauer*

*Institut für Experimentalphysik, Technische Universität Wien
A-1040 Wien, Austria*

The pressure response of Kondo lattices and heavy fermion systems is studied by means of resistivity and specific heat measurements as well as by L_{III} absorption-edge spectroscopy. Results are accounted for in the scope of NCA solutions of the Anderson model. Special emphasis is put on the mirror-like behaviour of Ce - in comparison to Yb systems.

I.- Introduction

Hydrostatic pressure applied to metallic and non-metallic compounds or alloys and in particular to Kondo lattices and heavy fermions can influence the ground state properties of such systems in a dramatic manner. Basically, this follows from the effect of pressure on microscopic quantities like the electronic density of states, the coupling constant, bandwidths, anisotropy parameters or magnetic moments. As an implication, characteristic temperature scales like the magnetic ordering temperature, the superconducting transition, the Kondo interaction strength, crystal field splitting or the metal-insulator transition will change, too.

Pressure experiments offer the unique possibility to distinguish between different interaction mechanisms present in these systems. This follows primarily from the pressure response of the various interaction mechanisms which can become either enhanced or weakened. Pressure also permits to calculate quantitatively microscopic parameters like the

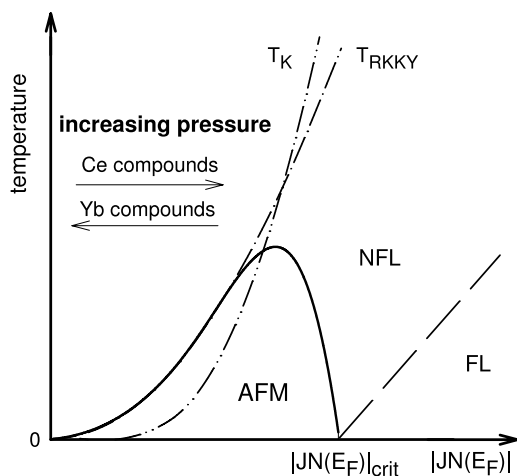
coupling constant times the electronic density of states at the Fermi energy or the Grüneisen parameter.

Magnetic properties of d or f materials are generally dominated from the $f-f$ or $d-d$ distance. This was firstly pointed out by Hill [1], who demonstrated the existence of a critical distance $d_{crit} \approx 3.2$ Å, which separates a local magnetic behaviour for $d_{f-f} > d_{crit}$ from itinerant magnetism for $d_{f-f} < d_{crit}$. A similar criterion was established by Schilling [2]. Both criterions imply that magnetism can easily be tuned by pressure via a change of the interatomic distances. However, one should keep in mind that for typical metals and compounds (with e.g., a bulk modulus $B_0 \approx 1000$ kbar) a change of 1 Å requires a pressure of 700 kbar. While many of such “tuning” experiments were carried out by appropriate chemical substitutions in order to vary interatomic distances, pressure as a “clean” thermodynamic quantity does neither introduce disorder nor changes the electronic structure of the system in an uncontrolled manner.

Beside the change of distances upon pressure, there is, in general, an increase of the valence of rare earth ions as an electron is squeezed out of the $4f$ -shell. This can cause intermediate valence, but leads in Kondo systems and heavy fermions based on cerium to a demagnetisation since $Ce^{3+}(4f^1) \rightarrow Ce^{4+}(4f^0)$, while for Yb based compounds and alloys the magnetic state is stabilised because of $Yb^{2+}(4f^{14}) \rightarrow Yb^{3+}(4f^{13})$.

The pressure induced strengthening of the magnetisation of Yb^{2+} is therefore the “mirror image” of the demagnetisation of Ce^{3+} which is known in the literature as the *electron-hole analogy* of Ce and Yb.

The actual ground state properties of Kondo lattices and heavy fermion compounds are determined from the mutual balance of the Kondo effect, RKKY interaction and crystal field splitting. For a given crystal field ground state multiplet, the magnetic behaviour is largely dictated by the parameter $|JN(E_F)|$, where J is the magnetic exchange coupling strength between conduction electrons and the $4f$ local moment and $N(E_F)$ is the density of conduction electron states at the Fermi energy. A qualitative understanding is derived from Doniach’s phase diagram [3], which is shown in figure 1. Depending on the absolute value of $|JN(E_F)|$ with respect to $|JN(E_F)|_{crit}$ the Kondo lattice can order magnetically for $|JN(E_F)| < |JN(E_F)|_{crit}$ but stays paramagnetic for



E. Bauer, figure 1

Figure 1: A schematic representation of Doniach’s model plotted as temperature vs. coupling constant times the conduction electron density of states $|JN(E_F)|$. $T_K \sim \exp[-1/(|JN(E_F)|)]$ and $T_{RKKY} \sim |J|^2 N(E_F)$. The dashed line separates the non-Fermi-liquid from the Fermi-liquid regime.

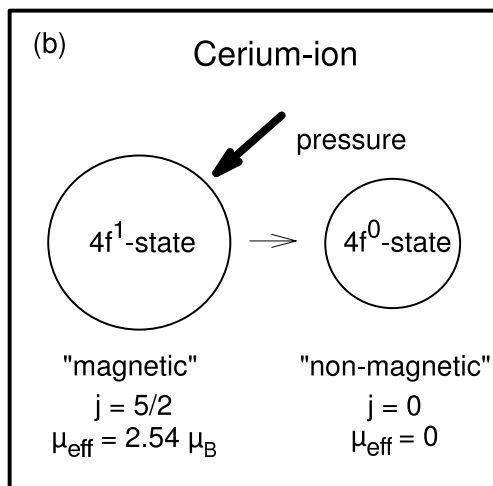
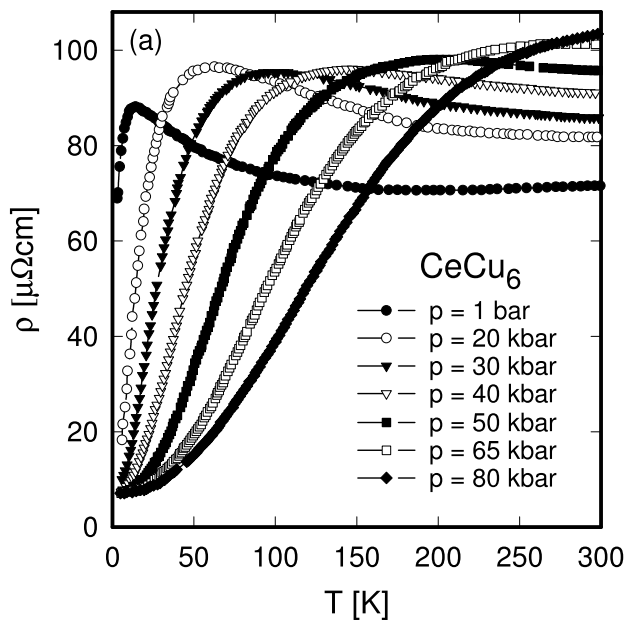
$|JN(E_F)| < |JN(E_F)|_{crit}$. Both regimes are separated by a quantum critical point (QCP). Significant deviations from Fermi-liquid properties frequently occur for systems which are driven towards the QCP. For an overview on the physics of non-Fermi-liquids, we refer to the lecture given by Castro-Neto at this summer-school. As pressure substantially modifies the value of $|JN(E_F)|$, systems can be shifted along the x-axis of Doniach's phase diagram. Pressure impels Ce compounds to larger values of $|JN(E_F)|$, thus, a transition from a magnetic to a non-magnetic state can be expected and the QCP is traversed from the magnetic side. Owing to the mirror-like behaviour of Yb compounds, pressure strengthens the magnetic state and therefore, a non-magnetic system can be driven towards the magnetic instability. In this case, the QCP is crossed from the non-magnetic regime.

Excellent surveys on the subjects indicated above can be found in the review articles of e.g., Schilling [4] and Thompson [5, 6] as well as in the Proceedings of the Santa Monica Workshop on non-Fermi-liquids [7].

II.- Pressure influence on microscopic - and macroscopic quantities of Ce and Yb systems

In order to demonstrate some of the unique features of pressure studies, a couple of experiments are shown and discussed in terms of solutions [8] of the Anderson model [9].

The mirror-like behaviour of Ce and Yb compounds becomes clearly evident from pressure dependent resistivity and specific heat measurements. The examples selected are CeCu₆ and YbCu₄Ag which are considered as typical Kondo lattices. CeCu₆ crystallises in the orthorhombic CeCu₆ structure but below 220 K [10] a monoclinic distortion takes place. This binary compound stays paramagnetic down to the mK range. The temperature dependent electrical resistivity ρ is displayed in figure 2(a) for various values of applied pressure. The data was taken from Kagayama et al. [11]. At ambient pressure CeCu₆ exhibits the well known behaviour of a Kondo lattice, i.e., at high temperatures ($T > 50$ K), $\rho(T)$ shows a logarithmic contribution due to independently acting Kondo scatterers, followed by a maximum at $T_\rho^{max} \propto T_K \approx 12$ K.

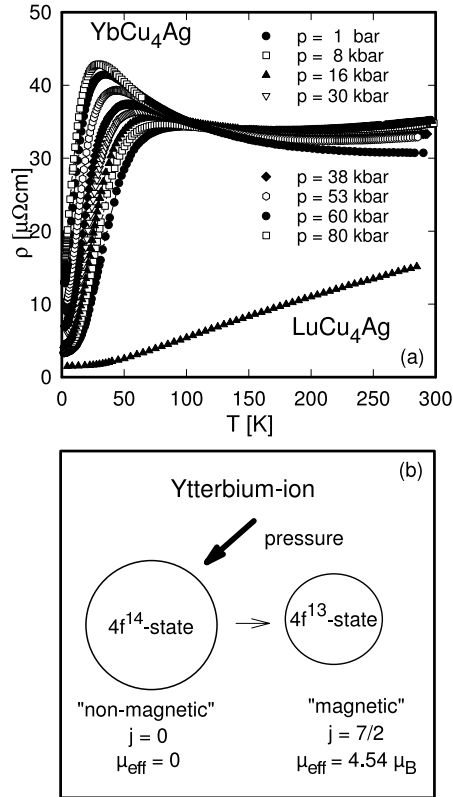


E. Bauer, figure 2

Figure 2: (a): Temperature and pressure dependent resistivity ρ of CeCu₆. (b): A sketch of the pressure response of the Ce³⁺ ion.

Well below this maximum CeCu₆ enters its coherent ground state reflected by a T^2 behaviour in $\rho(T) = \rho_0 + AT^2$, where the huge coefficient $A \approx 110 \mu\Omega\text{cm}/\text{K}^2$ [12] results from the significantly enhanced quasi-particle density of states at the Fermi energy. The absolute value of A , however, depends strongly on the sample quality. The overall $\rho(T)$ behaviour observed matches almost perfectly the theoretical predictions of Cox and Grewe [13] concerning temperature dependent quantities of Kondo lattices. Increasing values of pressure cause different responses: i) T_ρ^{max} grows substantially, thus reflecting an increase of T_K , which is derived from a growing hybridisation of the almost localised $4f$ electrons with the delocalised conduction electrons. ii) The coefficient A decreases, which is associated with a decrease of the density of states at $E = E_F$. The overall effect of pressure on Ce systems is basically the destabilisation of the magnetic $4f^1$ state since the Ce- $4f^1$ electron becomes progressively squeezed out of the $4f$ shell.

The temperature and pressure dependent resistivity of YbCu₄Ag is shown in figure 3(a) where the data was taken from reference [14]. This ternary compound crystallises in an ordered variant of the cubic AuBe₅ structure. At high temperatures, the negative logarithmic contribution to the total electrical resistivity renders a single impurity Kondo interaction of the conduction electrons with the almost localised Yb- $4f$ moments. At low temperatures, however, the ordered Yb sublattice allows a Bloch-like motion of the conduction electrons, and consequently the resistivity drops down. Both regimes are separated by a smooth maximum near 90 K with $T_\rho^{max} \propto T_K$ [13]. Therefore, YbCu₄Ag represents a Kondo lattice with a relatively high Kondo temperature. This induces a couple of important consequences for physical properties. Since T_K of YbCu₄Ag is large, the associated hybridisation prevents a lifting of the ground state degeneracy due to crystal field effects and the 8-fold degenerate state of the Yb ion ($j = 7/2$) operates in the whole temperature range. Moreover, as $T_K \gg T_{RKKY}$, long range magnetic order is unlikely and the system remains paramagnetic down to the mK range. Below 10 K the T^2 behaviour of $\rho(T)$ refers to a Fermi-liquid behaviour and the large coefficient $A = 8 \text{ n}\Omega\text{cm}/\text{K}^2$ [14] results from interactions with the heavy quasi-particle bands. An opposite “mirror-like” behaviour compared to CeCu₆ is found from the pressure response: Pressure causes both a decrease of T_ρ^{max} and

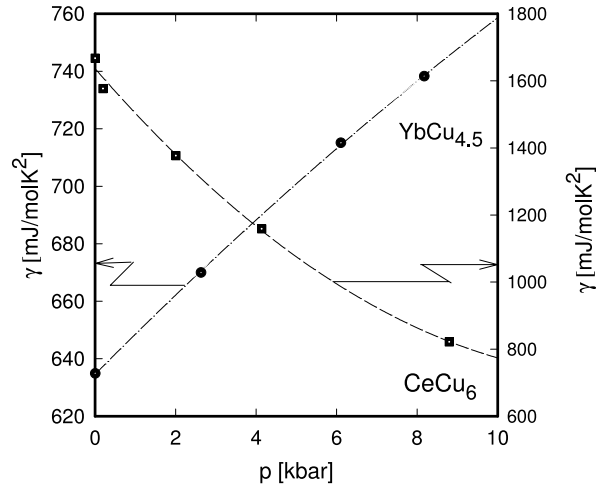


E. Bauer, figure 3

Figure 3: Temperature and pressure dependent resistivity ρ of YbCu₄Ag. (b): A sketch of the pressure response of the Yb²⁺ ion.

a significant increase of A . Now, the former indicates a lowering of T_K and the latter reflects the growing DOS at the Fermi energy. The total effect of pressure applied to Yb systems is therefore a stabilisation of the Yb magnetic moments.

Basically, this “mirror-like” behaviour can be understood from an electron - hole analogy of the electronic configurations (EC) of Ce and Yb, where the magnetic - and the non-magnetic state depend on the volume. In the case of Ce, the magnetic state $4f^1$ is the large one. Pressure applied to Ce ions will reduce the atomic volume by squeezing



E. Bauer, figure 4

Figure 4: Pressure dependent Sommerfeld coefficient γ of $\text{YbCu}_{4.5}$ (left axis) and CeCu_6 (right axis).

out the $4f^1$ electron. Hence, the non-magnetic small-volume EC $4f^0$ is progressively attained. In the case of Yb, the EC with the larger volume is the non-magnetic $4f^{14}$ state. Again, pressure will reduce the available volume by squeezing out one electron, which is synonymous with the creation of a hole in the f -shell as the small-volume magnetic $4f^{13}$ state is approached. A sketch of the opposite pressure responses of Ce and Yb ions is shown in figures 2(b) and 3(b).

Some corroboration for the scenario outlined above can be derived from pressure dependent specific heat studies. Results are shown for representative cerium and ytterbium examples (reference [15]) in figure 4, where the Sommerfeld coefficient γ is plotted as a function of pressure. While γ decreases for CeCu_6 , the opposite occurs in the case of $\text{YbCu}_{4.5}$. This indicates a lowering of the electronic density of states $N(E_F)$ at the Fermi energy for Ce systems. On the contrary, $N(E_F)$ is enhanced for the Yb compound.

In order to understand these distinct features from a more the-

oretical and quantitative point of view, solutions of the Anderson model with large Coulomb interactions are considered. In the scope of the non-crossing approximation the following expression is derived [8]:

$$n_f/(1 - n_f) = N_f\Delta/T_K, \quad (1)$$

where n_f is the number of $4f$ electrons in the case of Ce or the number of holes in the case of Yb. N_f is the ground state degeneracy and Δ is the hybridisation constant between $4f^1(ds)^3$ and $4f^0(ds)^4$ states for Ce or $4f^{14}(ds)^2$ and $4f^{13}(ds)^3$ states for Yb. Since the atomic radius $r_a(4f^1) > r_a(4f^0)$, the number of $4f$ electrons in Ce-compounds *decreases* with pressure. Therefore $N_f\Delta/T_K$ decreases as a whole. Oppositely, the atomic radius $r_a(4f^{13}) < r_a(4f^{14})$, consequently, the number of $4f$ holes in Yb-compounds *increases* with pressure as does $N_f\Delta/T_K$.

Pressure, however, influences both $N_f\Delta$ and the Kondo temperature T_K which can be written as [8]

$$T_K = D \exp(-\pi|\epsilon_f|/N_f\Delta), \quad (2)$$

with D the effective bandwidth and ϵ_f the binding energy of bare f -electrons (holes). Equation 2 demonstrates that the Kondo temperature varies exponentially; hence T_K changes more rapidly than does $N_f\Delta$. Therefore, if the number of electrons decreases T_K increases, too, but decreases if the number of holes increases. The pressure dependent variation of T_ρ^{max} of both CeCu₆ and YbCu₄Ag is shown in figure 5. As $T_\rho^{max} \propto T_K$ [13], equation 1 is directly proven from the experimental findings.

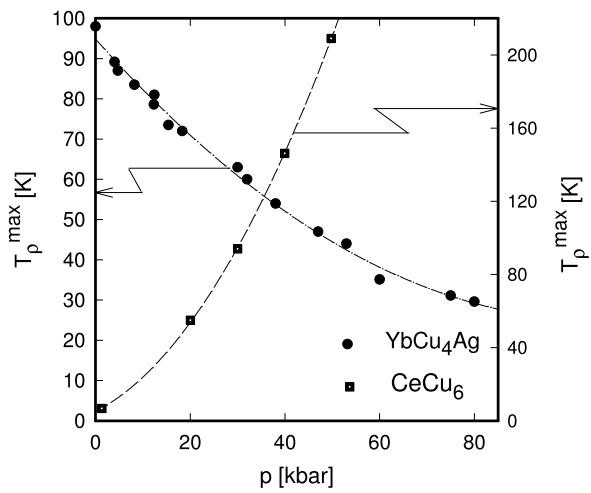
Besides, the pressure dependent change of T_K effects details of the Kondo resonance (ASR). In particular, the width Γ of the ASR is directly related to T_K via [8]

$$\Gamma = \pi T_K/N_f, \quad (3)$$

which causes the effective density of states $\rho_f(0)$ at E_F to become pressure dependent:

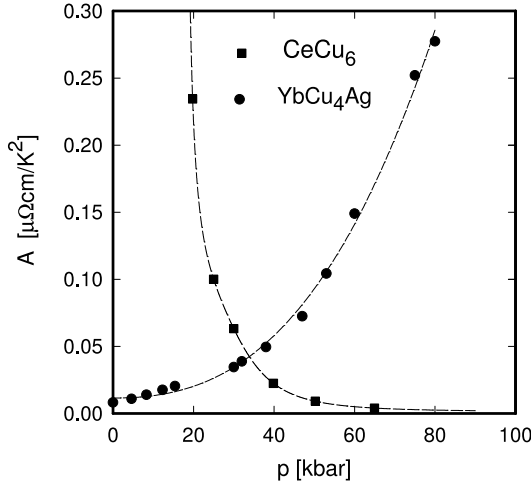
$$\rho_f(0) = 1/(\pi\Gamma) \sin^2(\pi n_f/N_f)|_{T=0}. \quad (4)$$

Physical quantities depending on the DOS at E_F like the electrical resistivity in the Fermi liquid regime or the Sommerfeld coefficient of the



E. Bauer, figure 5

Figure 5: Pressure dependent maximum temperature T_{ρ}^{max} of YbCu_4Ag (left axis) and CeCu_6 (right axis).



E. Bauer, figure 6

Figure 6: Pressure dependent variation of the resistivity coefficient A ($\rho = \rho_0 + AT^2$) of CeCu_6 and YbCu_4Ag .

specific heat can be accounted for in terms of equation 4; the pressure derived increase of T_K of cerium systems causes Γ to increase and thus $\rho_f(0)$ reduces. Therefore, the coefficient A of the resistivity and the γ value of the specific heat of typical cerium systems decrease, while these quantities, according to the electron-hole symmetry, rise when the pressure grows. In fact, the experimental data displayed in figures 6 and 4 evidence the model outlined above.

Since pressure significantly changes the Kondo interaction strength of a certain system, the mutual balance with other important interaction mechanisms becomes changed, too. In particular RKKY interaction and crystal field splitting can lose or gain weight in the case of Ce or Yb systems, respectively.

Starting from the generalised magnetic susceptibility [16]

$$\chi(q, \omega, T) = \frac{\chi_0(\omega, T)}{1 - J(q, \omega, T)\chi_0(\omega, T)}, \quad (5)$$

where χ_0 is the local magnetic susceptibility and $J(q, \omega, T)$ is the ex-

change integral, which couples fluctuating moments of a particular lattice site with others, and taking

$$\chi_0 = C/(T + T_K), \quad (6)$$

with C the Curie constant, leads for the marginal case $\omega \approx 0$ [16]:

$$\chi(q, 0, T) = C/(T + T^*). \quad (7)$$

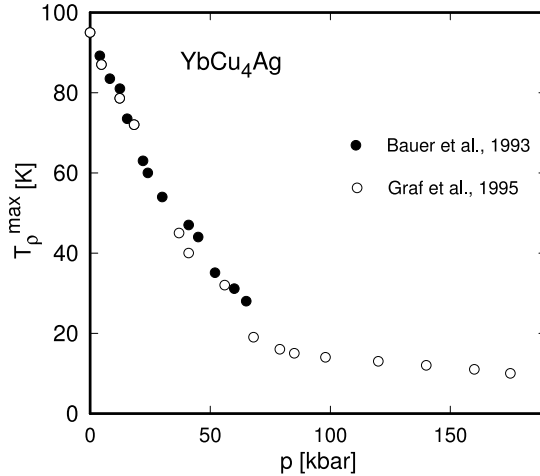
Equation 7 introduces a new temperature scale T^* , originated by the combined interaction of intersite magnetic correlations and the Kondo effect which is given by

$$T^* = T_K[1 - CJ(q, 0, T)/T_K]. \quad (8)$$

This model seems to contain a basic description of both high- and ambient-pressure results, moreover, T^* also is q -dependent. Several features can be derived from equation 8 [6]:

- $T_K > CJ(q, 0, T)$: the answer of the system results basically from the *pressure response of T_K* and is therefore very large.
- long range magnetic order is expected to occur for a critical, q -dependent value of J such that $CJ_c(q_c, 0, T) = T_K$. Above that limit, the system is dominated from *intersite interactions* and the pressure dependence is small.
- Equation 8 also explains why the Sommerfeld coefficient $\gamma \sim 1/T_0 \sim 1/T^*$ becomes very large near to a magnetic instability, i.e., when $CJ(q, 0, T) \leq T_K$.

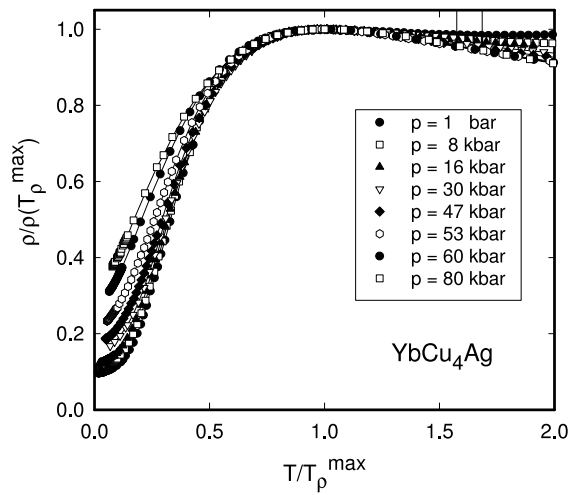
The change of the regimes from $T_K > CJ(q, 0, T)$ to $CJ_c(q_c, 0, T) \geq T_K$ can be observed experimentally from the pressure dependent variation of T_ρ^{max} of YbCu₄Ag (figure 7, data taken partly from reference [14, 17]). Initially, there is a substantial variation of $T_\rho^{max}(p)$ as $T_K \gg T_{RKKY}$. Since T_K lowers for typical Yb systems as a function of pressure, both scales approaches each other at elevated loads, and eventually $CJ(q, 0, T) > T_K$. This causes that intersite interactions dominate and consequently the pressure response becomes very small.



E. Bauer, figure 7

Figure 7: Pressure dependent maximum temperature T_{ρ}^{max} of YbCu_4Ag .

Due to the pressure dependent change of T_K , crystal field interactions can become the primary effect present in cerium and ytterbium systems. In the case of YbCu_4Ag , T_K is of the order of 100 K, thus larger than the overall crystal field splitting Δ_{CF} as e.g. derived for the isoelectronic compound YbCu_4Au [18]. In such a case, the total angular momentum ($j = 7/2$ for Yb) operates in the whole temperature range and determines the ground state properties. However if T_K is diminished due to the applied pressure, Δ_{CF} becomes comparable and finally one arrives with $\Delta_{CF} \gg T_K$. The total angular momentum is then no longer preserved, since the crystal field with cubic symmetry removes the 8-fold degeneracy and leaves a doublet as ground state. This modifies most of the physical properties and T_K can no longer be treated as the dominating scale. Experimentally, this can be seen e.g., from a scaling behaviour of the pressure dependent electrical resistivity of YbCu_4Ag . As long as the Kondo effect dominates as *the* single energy scale of the system, the data scales when plotted according to $\rho/\rho(T_{max})$ vs T/T_{max} (compare figure 8, data taken from reference [14]). Such a scaling behaviour holds



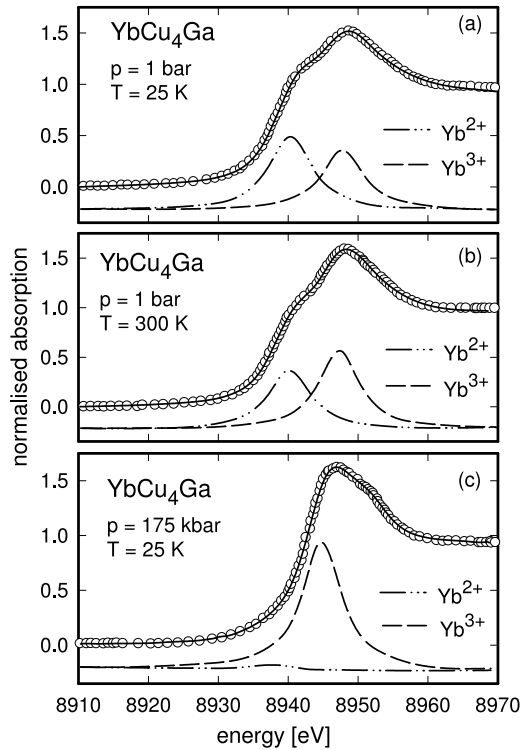
E. Bauer, figure 8

Figure 8: Scaling of the temperature and pressure dependent resistivity of YbCu₄Ag.

up to about 20 kbar. Above about this pressure range, T_K is reduced to $T_K \approx \Delta_{CF}$, causing that T_K is no longer the only energy scale of the system. Therefore, scaling breaks down as it is evidenced by significant deviations of the data from a virtual single line, which would correspond to the usual scaling properties of a certain physical quantity.

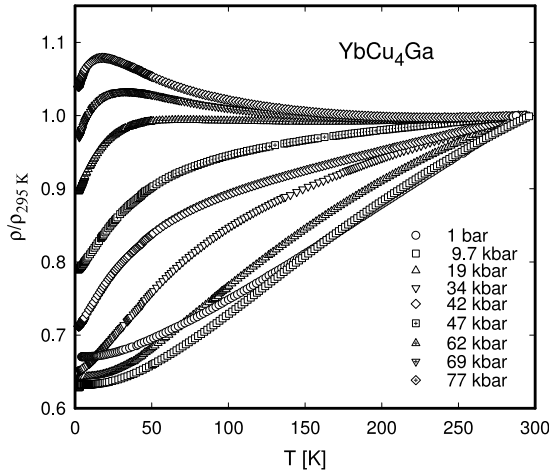
Beside the already mentioned interaction mechanisms present in strongly correlated electron systems, valence can play a crucial role. This refers to the fact that the number of electrons or holes, n_f , enters the most significant equations like equations 1 or 4 and thus determines the ground state properties of a system. For proper Ce and Yb compounds and alloys, the valence is, at least partly, adjustable by pressure from the 3+ towards the 4+ state in the former and from 2+ towards the 3+ state in the latter. As an intermediate stage, intermediate valence can occur, resulting from a quantum mechanical mixture of the two consecutive states. To illustrate such a tuning of the valence, pressure dependent L_{III} absorption edge - and resistivity measurements are shown in figures 9 and 10 for YbCu_4Ga [19, 20]. This compound crystallises in the hexagonal CaCu_5 structure and the valency at ambient conditions is $\nu \approx 2.5$. This is reflected from an almost equal spectral weight of the Yb^{2+} and the Yb^{3+} state (figure 9(a)). As soon as pressure is applied, spectral weight shifts towards the 3+ state (compare figure 9(c)) and the valency increases. Eventually $\nu = 2.96$ for $p = 150$ kbar. Contemporaneously, there is a remarkable change of the temperature dependent resistivity. While for small values of applied pressure, $\rho(T)$ grows continuously with temperature, increasing load causes a strong curvature to occur and eventually, a maximum develops which shifts further towards lower temperatures.

This almost text-book-like feature is interpreted as the crossover from intermediate valence for small pressure towards a typical Kondo lattice behaviour for sufficiently large hydrostatic pressure, when the trivalent state of the Yb ion is approached. Equivalently, this behaviour can be explained in terms of a transition from a “high Kondo temperature” system at ambient pressure, towards a “low Kondo temperature” system at elevated values of pressure which impels a significant alteration of the degree hybridisation and hence the deviation from an integer valence state.



E. Bauer, figure 9

Figure 9: Pressure and temperature dependent L_{III} absorption edge spectra of YbCu_4Ga . The dashed and the dashed-dotted line represent the Yb^{3+} and the Yb^{2+} contribution, respectively.



E. Bauer, figure 10

Figure 10: Pressure and temperature dependent resistivity ρ of YbCu_4Ga .

III.- Grüneisen analysis

Scaling behaviour and the relationship between experimental quantities follow from combining thermodynamics with the assumption that the free energy obeys a scaling law [5]: $F = F_0(T, V) + F_e(T, V)$ where the electronic contribution $F_e(T, V) = Nk_B T f(T/T_0(V))$ and where N is the number of atoms and T_0 is the characteristic temperature (e.g., T_K , T_{sf} or $T_{\nu f}$). The key magnitude of this analysis is the electronic Grüneisen parameter

$$\Omega_e = -\frac{\partial \ln T_0}{\partial \ln V} = B_0 \frac{1}{T_0} \frac{\partial T_0}{\partial p} \quad (9)$$

with the bulk modulus B_0 . The particular relationships between the pressure derivatives of various physical quantities are inferred from a scaling assumption based on the predominant volume dependence of the characteristic temperature T_0 . From an assumed scaling with T_0 , the logarithmic volume derivatives of the low temperature quantities χ , C_p

and ρ are interrelated through Ω_e .

$$\chi(0) \sim 1/T_0 \Rightarrow \frac{\partial \ln \chi}{\partial \ln V} \equiv \Omega_\chi = \Omega_e, \quad (10)$$

$$\begin{aligned} \rho(T) - \rho_0 &\sim AT^2 \sim \left(\frac{T}{T_0}\right)^2 \\ \Rightarrow \frac{\partial \ln \rho}{\partial \ln V} &\equiv 2\Omega_A = 2\Omega_e, \end{aligned} \quad (11)$$

$$\begin{aligned} C_p(T) = \gamma T &\sim \frac{T}{T_0} \\ \Rightarrow \frac{\partial \ln \gamma}{\partial \ln V} &\equiv \Omega_c = \Omega_e, \end{aligned} \quad (12)$$

Hence, the Grüneisen analysis correlates the measurements of the pressure (volume) dependence of many quantities to the ambient pressure data of the specific heat C_e and the thermal expansion β_e , given that a single energy scale is valid, i.e.,

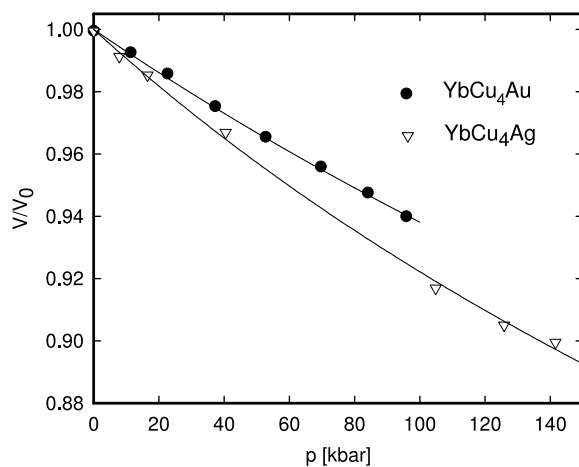
$$\Omega_e = \frac{\beta_e V B_0}{C_e}. \quad (13)$$

The bulk modulus B_0 can be evaluated from pressure dependent measurements of the lattice constants considering Murnaghan's equation of state [21]

$$\frac{V_0 - V}{V_0} = 1 - \left(\frac{B_0^*}{B_0} p + 1\right)^{-1} 1/B_0^* \quad (14)$$

with B_0^* as the derivative of B_0 . V and V_0 are the volumes with and without pressure p , respectively. As an example, the pressure dependent variation of the lattice parameter a is shown for YbCu₄Ag and YbCu₄Au (reference [14] and [22], respectively) in figure 11. From least squares fits according to equation 14, the following parameters are derived: YbCu₄Au: $B_0 = 1400$ kbar, $B_0^* = 3.5$, YbCu₄Ag: $B_0 = 1080$ kbar, $B_0^* = 3.3$.

Considering equation 9 and the bulk modulus B_0 derived experimentally, as well as the pressure response of YbCu₄Ag with $\partial T_\rho^{max}/\partial p \approx$



E. Bauer, figure 11

Figure 11: Pressure dependent variation of the lattice constant A of YbCu_4Ag and YbCu_4Au . The solid line is a least squares fit according to Murnaghan's equation of state.

-1.8 K/kbar and $T_\rho^{max} \propto T_0$, the Grüneisen constant $\Omega_e = -20$. A similar analysis performed for CeCu₆ reveals $\Omega_e = 57$ [23]. The negative Grüneisen parameter observed for YbCu₄Ag and the positive one for CeCu₆ obviously reflect the electron-hole analogy of Ce and Yb systems again. The extraordinary large values of Ω_e of Kondo lattices and heavy fermion systems demonstrate the significant influence of volume on electronic properties of such systems which are primarily determined by a single energy scale in certain parameter ranges.

IV.- Summary

The physics of Kondo - and heavy fermion systems is, in general, determined by a small energy scale, typically of the order of 10 to 100 K. External parameters like temperature, magnetic fields or pressure thus can extraordinarily effect properties of these materials. The latter is responsible for a reduction of the lattice spacings and thereby of a change of the electronic structure near to the Fermi energy as well as for an increase of the system's valence.

Changes of electronic parameters will alter the ground state properties of such compounds and Ce or U systems can undergo a magnetic to non-magnetic transition. The opposite occurs for Yb compounds due to the electron-hole analogy. This phenomenon has numerously been proven for Ce compounds, but only recently a cross-over from the non-magnetic - to the magnetic state has been observed for Yb compounds [24, 25, 27].

In the vicinity of the magnetic instability, strong spin fluctuations cause a breakdown of the expected Fermi-liquid features which can be studied in detail by a pressure driven tuning of the most relevant parameters of the systems, i.e., $|JN(E_F)|$. In fact, some of the most exciting phenomena near to a quantum critical point like the occurrence of superconductivity were established from pressure related experiments [26]. Moreover, since critical spin fluctuations are suppressed by pressure, a Fermi liquid ground state can be recovered.

V.- Acknowledgements

This work has been supported by the Austrian Science Foundation, (projects P 12899 and 13544). I am grateful to P. Bonville, M. Ellerby, P. Fischer A. Galatanu, R. Hauser, G. Hilscher, F. Marabelli, H. Michor, L. Naber and J. Sereni for their valuable contributions.

References

- [1] H.H. Hill, in *Plutonium 1970 and other Actinides*, edited by W.N. Miner, (Metallurgical Society of the American Institute of Mining, New York 1970) p.2
- [2] J.S. Schilling, Mat. Res. Soc. Symp. Proc. **22**, 79 (1984).
- [3] S. Doniach, Physica **B 91**, 231 (1977).
- [4] J.S. Schilling, Adv. Phys. **28**, 657 (1979).
- [5] J.D. Thompson and J.M. Lawrence, in *Handbook on the Physics and Chemistry of Rare Earths*, Vol. 19, edited by K.A. Gschneidner Jr. and L. Eyring, (Elsevier 1994) p.383.
- [6] J.D. Thompson, in *Frontiers in Solid State Sciences, Vol 2*, edited by L.C. Gupta and M.S. Multani, (World Scientific, London, New Jersey, London, Hong Kong, 1993) p. 107.
- [7] J. Phys.: Cond. Mat. **8**, 9871 (1996).
- [8] N.E. Bickers, D.L. Cox, and J.W. Wilkins, Phys. Rev. **B 54**, 230 (1987).
- [9] P.W. Anderson, Phys. Rev. **121**, 41 (1961).
- [10] E. Gratz, E. Bauer, H. Nowotny, H. Müller, S. Zemirli, and B. Barbara, Physica B **63 - 64** 312 (1987).
- [11] T. Kagayama and G. Oomi, in *Transport and Thermal Properties of f-electron Systems*, edited by G. Oomi, H. Fuji and T. Fujita (Plenum, New York, 1993), p. 155.

- [12] H.R. Ott, H. Rudigier, Z. Fisk, J.O. Willis, and G.R. Stewart, *Solid State Commun.* **53**, 235 (1985).
- [13] D. Cox and N. Grewe, *Z. Phys. B* **71**, 321 (1988).
- [14] E. Bauer, R. Hauser, E. Gratz, K. Payer, G. Oomi, and T. Kagayama, *Phys. Rev. B* **48**, 15873 (1993).
- [15] A. Amato, R.A. Fisher, N.E. Phillips, D. Jaccard, and E. Walker, *Physica B* **165 - 166**, 389 (1990).
- [16] C.J. Pethick and D. Pines, in *Recent Progress in Many-Body Theories*, ed. A.J. Kallio, E. Pajanne and R.F. Bishop (Plenum, New York, 1988) p. 17.
- [17] T. Graf, R. Movshovich, J.D. Thompson, Z. Fisk, and P. Canfield, *Phys. Rev. B* **52**, 3099 (1995).
- [18] A. Severing, A.P. Murani, J.D. Thomson, Z. Fisk, and C.K. Loong, *Phys. Rev. B* **41**, 1739 (1990).
- [19] R. Luebbers, J. Dumschat, G. Wortmann, and E. Bauer *J. Physique IV Colloque* **7(C2)**, 1021 (1997).
- [20] E. Bauer, Le-Tuan, R. Hauser, E. Gratz, T. Holubar, G. Hilscher, H. Michor, W. Perthold C. Godart, E. Alleno, and K. Hiebl, *Phys. Rev. B* **52**, 4327 (1995).
- [21] F.D. Murnaghan, *Finite Deformation of an Elastic Solid*, (Dover, New York, 1951) p. 68
- [22] E. Bauer, E. Gratz, R. Hauser, A. Galatanu, A. Kottar, H. Michor, W. Perthold, T. Kagayama, G. Oomi, N. Ichimiaya and S. Endo, *Phys. Rev. B* **50**, 9300 (1994).
- [23] A. deVisser, A. Lacerda, P. Haen, J. Flouquet, F.E. Kayzel, and J.J.M. Franse *Phys. Rev. B* **39**, 11301 (1989).
- [24] H. Winkelmann, M.M. Abd-Elmeguid, H. Micklitz, J.P. Sanchez, P. Villet, K. Alami-Yadri, and D. Jaccard, *Phys. Rev. B* **60**, 3324 (1999).

-
- [25] O. Trovarelli, C. Geibel, and F. Steglich, *Physica B*, (1999) in press.
- [26] N.D. Mathur, F.M. Grosche, S.R. Jialn, I.R. Walker, D.M. Freye, R.K. Haselwimmer and G.G. Lonzarich, *Nature*, **394**, 39 (1999).
- [27] E. Bauer, A. Galatanu, L. Naber, M. Galli, C. Seuring, K. Heuser, E.W. Scheidt, T. Schreiner, and G.R. Stewart, *Physica B*, (1999) in press.

X-ray Absorption Spectroscopy of Strongly Correlated Electron Systems

Jesús Chaboy Nalda

Instituto de Ciencia de Materiales de Aragón (I.C.M.A) & Departamento de Física de la Materia Condensada, C.S.I.C.-Universidad de Zaragoza, C/ Pedro Cerbuna 12, 50009 Zaragoza, Spain

In the past few years, the advent of intense, tuneable, polarized synchrotron radiation sources has stimulated world-wide interest in using x-rays to address magnetic aspects in the electronic structure and magnetism of condensed matter. Special attention has been paid to x-ray magnetic circular and linear dichroism (XMCD, XMLD) in core level photoabsorption because it has revealed as a unique element-selective magnetic probe. To this respect, the derivation of the sum rules for the dichroic signal, showing the relationship of the XMCD to the local spin and orbital magnetic moments constitutes a critical success in the development of the field.

In this talk a review is given of the principles underlying x-ray absorption and x-ray magnetic circular and linear dichroism spectroscopies. The main strengths of these techniques mainly focused on strongly correlated electron systems are highlighted. Finally, a survey of the possibilities offered by spin-dependent near-edge x-ray magnetic techniques (of separately probing a given element, electronic shell, and crystallographic site in a material containing several magnetic species) to disentangle a wide set of problems on the magnetism of materials is illustrated by showing different selected examples.

I.- Introduction

In the past few years, the advent of intense, tuneable, polarized synchrotron radiation sources has stimulated world-wide interest in using x-rays to address magnetic aspects in the electronic structure and magnetism of condensed matter. Special attention has been paid to x-ray magnetic circular and linear dichroism (XMCD, XMLD) in core level photoabsorption because it has revealed as a unique element-selective magnetic probe. To this respect, the derivation of the sum rules for the dichroic signal, showing the relationship of the XMCD to the local spin and orbital magnetic moments, constitutes a critical success in the development of the field.

Our purpose here is to present a brief review of the principles underlying x-ray absorption and x-ray magnetic circular and linear dichroism spectroscopies. The main strengths of these techniques mainly focused on strongly correlated electron systems are highlighted. Finally, a survey of the possibilities offered by spin-dependent near-edge x-ray magnetic techniques (of separately probing a given element, electronic shell, and crystallographic site in a material containing several magnetic species) to disentangle a wide set of problems on the magnetism of materials is illustrated by showing different selected examples.

II.- X-ray Absorption Spectroscopy (XAS): basic principles.

The basic process of X-ray absorption is the excitation of electrons from deep core levels of a selected atom by the absorption of a photon.

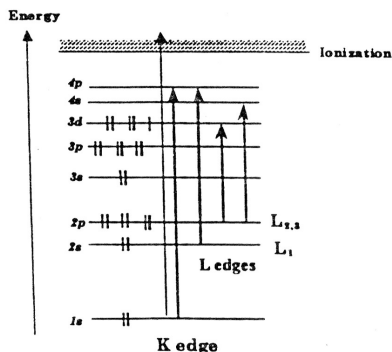


Figure 1. Scheme of the excitation of an electron by the absorption of a x-ray photon.

Core state	Spectroscopic name
1s	K
2s, 2p	L ₁ , L _{2,3}
3s, 3p, 3d	M ₁ , M _{2,3} , M _{4,5}
4s, 4p, 4d, 4f	N ₁ , N _{2,3} , N _{4,5} , N _{6,7}

When X-rays pass through any sort of material, a proportion of them will be absorbed. (The attenuation of x-rays by matter generally follows the relation $I=I_0e^{-\mu x}$, where μ is the x-ray absorption coefficient, and x is the sample thickness)¹. The absorption of x-rays by atoms is smoothly varying with photon energy except at some discrete energies where abrupt increases occur, called absorption edges. These edges correspond to the x-ray photon attaining enough energy to free or excite a bound electron in the atom.

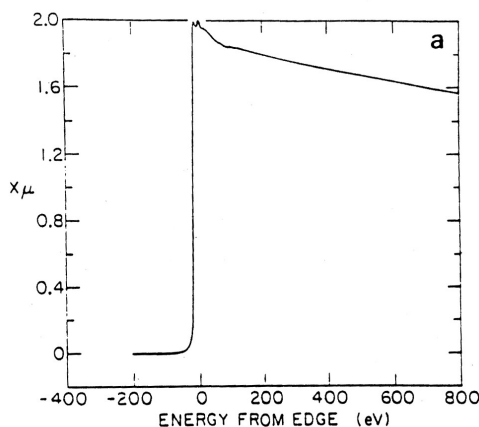


Figure 2a. The x-ray absorption coefficient, $x\mu$, times thickness, x , of isolated krypton atoms in the vapour form.

The absorption of x-rays on the high energy of the absorption edges does not vary monotonically in condensed matter but has a complicated behavior which extends past the edge by an amount typically of the order of 1 keV. The small oscillations can superimposed on the edge step gradually die

away as the X-ray energy increases. The oscillations are known as EXAFS (Extended X-ray Absorption Fine Structure) are due to the interaction of the photoelectron with the surrounding atoms.

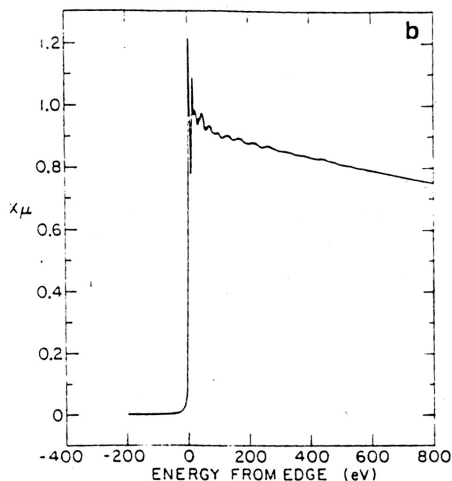


Figure 2b. The x-ray absorption coefficient, μ , times thickness, x , of one monolayer of krypton adsorbed on Grafoil².

Usually the x-ray absorption spectrum is divided in several regions depending on the energy of incoming photons:

- * the pre-edge, edge and the near-edge (XANES) regions, which extend about 20 eV below the edge to 30-100 beyond the edge.

- * the EXAFS region which extends from 30-100 eV to 600-1000 eV beyond the edge.

The physical origins of the absorption features in the pre-edge and edge regions depend on the material, i.e. Rydberg states in free atoms, bound valence states or bound multiple scattering resonances in molecules, unoccupied local electronic states in metals and insulators. Thus, analysis of these near-edge features in the spectrum of a particular sample can provide information about vacant orbitals, electronic configuration and the site symmetry of the absorbing atom.

The underlying physics of the processes that occur to produce the XANES and EXAFS structures in the x-ray absorption spectra is easy to understand. The photon is completely absorbed and kicks out a core photoelectron from the absorbing atom leaving behind a core hole. This photoelectron

will be ejected with an energy equal to energy of the incoming photon less its binding energy, when in the core. This photoelectron will interact with the surrounding atoms. Considering the wave nature of the ejected photoelectron and regarding the atoms as point scatterers a simple picture can be seen in which the backscattered waves interfere with the forward wave to produce either peaks or troughs. This is an interference effect on the final state. Since the transition probability is given by a matrix element between the final and initial states and the absorption coefficient is related to the transition probability, this interference affects the absorption coefficient which is the value that is measured in an XAS experiment.

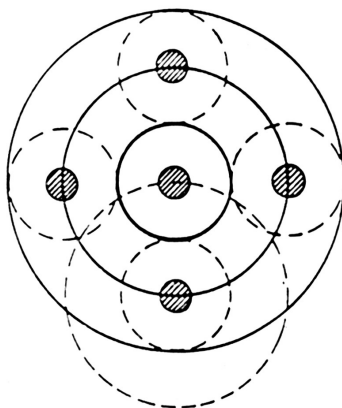


Figure 3. Illustrating the interference of the scattered photoelectron wavefunction by the neighbouring atoms with its outgoing portion.

The wavelength of the photoelectron is dependent on its energy and thus the phase of the back scattered wave at the central atom will change with the energy of the incoming photon. This leads to the oscillatory nature of the interference effect. Since backscattering amplitude and phase are dependent on the type of atom doing the backscattering and the distance it is from the central atom, information regarding the coordination environment of the absorbing atom can be obtained by analysing the XANES and EXAFS. The only distinction between XANES and EXAFS regions is the relative weight of the multiple scattering processes of the excited photoelectron. Usually it is considered that in the EXAFS region only single-scattering processes are important contrary to the XANES region in which due to the low kinetic energy of

the ejected photoelectron multiple scattering processes are dominant. Consequently, through careful analysis of the oscillating part of the spectrum after the edge, information relating to the coordination environment of a central excited atom can be obtained.

1. X-ray Absorption Spectroscopy and Synchrotron Radiation.

One of the fundamental reason why the development of XAS started at the end of the 70's is experimental and it is linked to the advent of intense, tuneable, polarized synchrotron radiation sources.

1) *What is Synchrotron Radiation?*

Light, in its original interpretation, refers to the part of the electromagnetic spectrum that is accessible to the eye. It is only a small portion of the complete electromagnetic spectrum. The waves are denoted as radio waves, micro waves, ultraviolet rays, X-rays or cosmic rays. Every type of radiation is, in a broader sense, light. To be able to "see" that which was denied the eye by nature has always been an innate goal of research. Success of a "visible discerning" experiment depends on how one manages to focus light of the correct wavelength with high enough intensity on a specimen. Synchrotron radiation makes such a seeing process possible. It is an intensive source of radiation.

Synchrotron radiation arises due to the motion of light elementary particles that are charged, e.g. electrons that approach the speed of light and are diverted sideways in their trajectories by a magnet. Synchrotron radiation is always given off in the forward direction, much like water droplets are thrown off from a rotating car tyre. The radiation is observed in the laboratory as a small light cone along the trajectory of the electron. The higher the kinetic energy of the particles, the stronger the light is collimated and the higher is the energy content of the light.

2) *Properties of synchrotron radiation*³.

Synchrotron radiation is superior to conventional radiation sources like X-ray tubes, with respect to several properties. It is without competition in a broad region of the electromagnetic spectrum from the ultraviolet up to

hard X-rays. The dominating property of synchrotron radiation lies in its high intensity, which is available over a broad region of the spectrum. This is of tremendous importance for the experimentalist. This is why an increase in usable intensity is the predominant objective in the planning and the construction of new sources of radiation.

The emitted radiation has a high intensity and is continuous over a broad spectral band which means it comprises radiation of different wavelengths. A light source with only one wavelength, a monochromatic source, is usually required by the scientists carrying out the experiments. This is achieved with the aid of monochromators, which are adjusted to the wavelength required; and can be varied throughout the course of the experiments as needed. The connection of wideband synchrotron radiation with a monochromator results in a continuously tuneable radiation source with high intensity. Many experiments can be performed simultaneously because several monochromators receive light from the storage ring.

Another one of the more remarkable properties of synchrotron radiation is its strong collimation and the small size of the source. Moreover, in contrast to other light sources synchrotron radiation can be calculated with high precision. This is an indispensable prerequisite to calibrate detectors and other radiation sources. The electrons which circulate in the ring do so in bunches. Then, the synchrotron radiation has a time structure defined by the electron bunches: short, intense flashes of light are emitted. Thus processes in the atomic area can be temporally observed.

One more invaluable property to individuals carrying out experiments is that the creation and handling of synchrotron radiation occurs solely in an ultra-high vacuum (UHV).

Synchrotron radiation is highly polarized. In the orbital plane the electric field vector of the emitted radiation is in the direction of the instantaneous acceleration. Thus radiation from bending magnets is linearly polarized in the plane of the orbit. Out of the orbit plane the polarization becomes elliptical and eventually circular, with opposite helicity above and below the plane. However, to get some circularly polarized intensity, the observer has to move out of the orbital plane at the price of a weak flux. To do circular dichroic experiments, it is necessary to move up and down the experiment with respect to the orbital plane. This disadvantage can be overcome by using radiation emitted from multipole insertion devices. These devices are periodic arrays of permanent magnets, so-called wigglers and undulators, installed in

the straight sections of the storage ring. They force the electrons to oscillate with a period of a few centimetres over a length of several metres. Each wiggler emits synchrotron radiation in the same forward direction. Thus the intensities from each wiggle are superimposed. The more wiggles the electrons pass the higher the resulting light intensity. In undulators interference effects contribute to further enhance the intensity.

Regular wigglers and undulators do not produce c.p.l. since contributions of right and left handed half periods, which positive and negative curvatures, do cancel. Several exotic designs have been proposed in the last years to bypass this limitation: helical undulator, asymmetric wiggler, crossed undulator, multipole wiggler, etc., designed with the aim of producing a fully polarized beam along the axis of the device. (In other words, if the magnetic fields in a wiggler and undulator are confined to one transverse plane, the alternating poles cancel this elliptical polarization out of the plane and the radiation is linearly polarized everywhere. For insertion devices with helical magnetic fields the radiation is elliptically polarized).

2. X-ray Absorption Spectroscopy (XAS): Fermi's Golden Rule.

The earliest approach to the description of x-ray absorption spectra employs the single-electron model as a starting point. In this picture, the core-electron is excited in the unoccupied continuum states of the system. According to Fermi's Golden Rule the transition probability per unit of time from a bound state to a continuum state can be written as

$$W = \frac{2\pi}{\hbar} |\langle k | \mathbf{P} | c \rangle|^2 \rho_f(\hbar\omega - E_c) \quad (1)$$

where $|\langle k | \mathbf{P} | c \rangle|$ is the matrix element of the electromagnetic field operator \mathbf{P} between the core-electron state $|c\rangle$ and the valence state $|k\rangle$, $\rho_f(E)$ is the density of valence states at the energy E above the Fermi level and E_c is the core-electron binding energy.

The operator \mathbf{P} can be written as

$$\mathbf{P} = e \frac{i\omega \vec{n} \cdot \vec{r}}{c} (\vec{p} \cdot \hat{e}) \quad (2)$$

where \mathbf{n} is the light propagation vector, $\hat{\mathbf{e}}$ the polarization vector, and \mathbf{r} and \mathbf{p} are the electron position and momentum operators. It is customary, and usually valid, to make the electronic dipole approximation, wherein the exponential is replaced by unity, giving

$$|\langle k|\mathbf{P}|c\rangle| \sim |\langle k|\hat{\mathbf{p}}, \hat{\mathbf{e}}|c\rangle| \quad (3)$$

In the dipole approximation \mathbf{P} can be replaced by \mathbf{P}_q , where q accounts for the polarization of the light: if it is linearly polarized along the quantization axis, then $q=0$, left and right circularly have $q=+1$ and $q=-1$, respectively. Since the electric dipole operator is odd and acts on the radial part of the electronic wave-function only (the x-ray photon carries angular momentum one and no spin), transitions can be made only between states which have opposite parity and differ in angular momentum by one: $\Delta l = \pm 1$ with $\Delta s = 0$, **the dipole selection rules**.

When XAS is performed with polarized x-rays, some extra selection rules have to be taken into account, thus extending the range of information available from this technique. These additional selection rules are at the origin of dichroism, i.e. of the polarization dependence of the absorption spectrum.

III.-X-ray Absorption in the lanthanides

1. $L_{3,2}$ and L_1 absorption in the lanthanides⁴.

The absorption of x-rays by excitation of lanthanide 2p electrons ($L_{3,2}$ -edges) is a simple and sensitive probe of the unoccupied lanthanide 5d states. These spectra are characterised by exhibiting a pronounced peak at the absorption threshold, that corresponds to the atomic-like $2p \rightarrow 5d$ transitions, usually referred as the "white-line". Changes in the shape of the white lines with increasing atomic number are determined by the localisation and hybridisation of the d unoccupied states and by the progressive filling of the d-band.

It should be noted that in the lanthanides two transitions are expected to occur in the excitation of a core electron from the 2p level according to the dipole selection rules: $2p \rightarrow 5d$ and $2p \rightarrow 6s$. However, the ratio between the $p \rightarrow d$ to $p \rightarrow s$ channels is found to be less than 3%, so that we can consider that the contribution to the $L_{3,2}$ absorption spectra coming from transitions to s-

like states is negligible as compared to the $p \rightarrow d$ channel, so that in the following we only deal with the main $p \rightarrow d$ transition.

Lanthanide $L_{3,2}$ absorption can be accounted by treating atomic absorption below the ionisation (discrete line spectrum) and the continuum absorption above the ionisation threshold separately. Usually, $L_{3,2}$ spectra can be reproduced as due to the superposition of $2p \rightarrow nd$ absorption lines and an arctan function curve representing the continuous absorption.

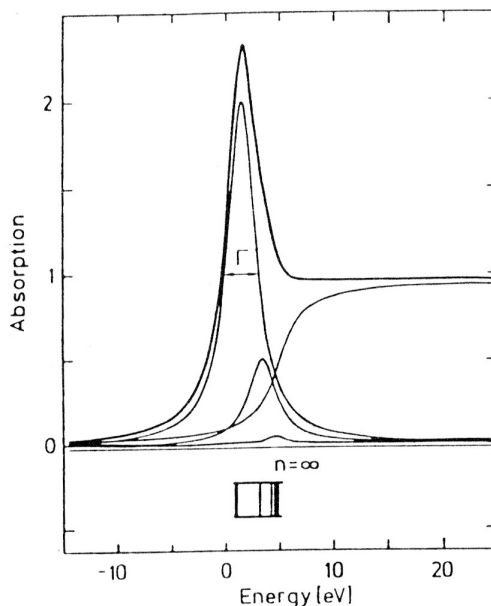


Figure 4. Deconvolution of Lanthanide $L_{3,2}$ absorption.

On the other hand, the spectral shape of the L_1 -edge spectra in all the lanthanide metals exhibits a step-like rise of the absorption at the threshold, reflecting the p -projected density of states in the band structure of the conduction electrons. However, in the case of condensed systems a shoulder-like feature appears at the threshold, as a consequence of the hybridisation of these p -states with the outer s - and d -symmetry orbitals. Therefore, the combined study of the L_3 and L_1 absorption edges in lanthanide materials can provide an unique insight to the understanding of localisation and hybridisation phenomena occurred in strongly correlated materials.

2. L-edge absorption in elemental lanthanides: vapours vs metals.

It is instructive to compare x-ray absorption of the elements in the gaseous state with the absorption in the condensed metallic state. The comparison between the L_3 absorption spectra of Ce in the vapour state (at 2500 K) and in the solid state at room temperature is shown in Fig. 5 . The spectrum in the gaseous state exhibits a pronounced peak followed by a rather structureless continuous absorption. Upon condensation into the metallic state the L_3 white-line does not vanish as one might most naively expect from the formation of a 5d band with free conduction electron. Instead the atomic absorption line remains largely intact: it is merely broadened and acquires a somewhat distorted, asymmetrical shape, indicating that the 5d states conserve strongly their atomic character upon condensation. However, the overlap of the 5d wavefunctions with neighbouring atoms, i.e. the hybridisation or the chemical binding, causes a characteristic variation of the atomic spectral shape. Therefore, the height of the L_3 white-line can be directly related to the localisation of the 5d states. This is shown in Fig. 5 where the L_3 absorption of La in

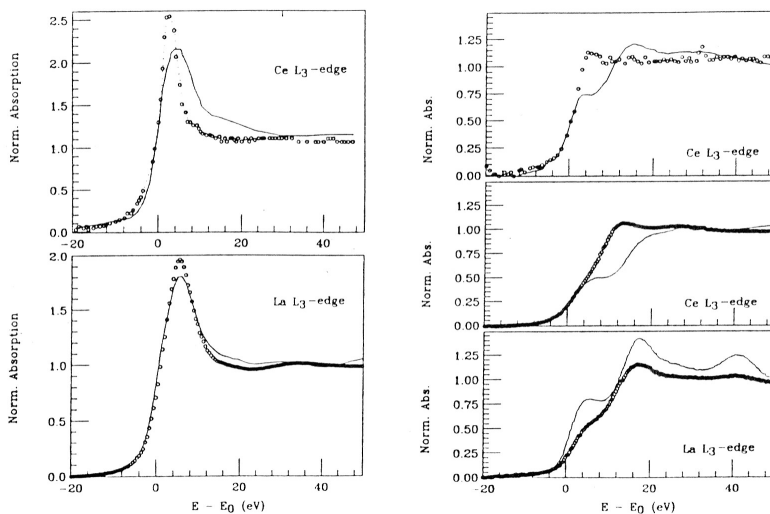


Figure 5. a) Top panel: L_3 -edge x-ray absorption of Ce in the vapour state (dots) at 2500 K and in the solid state (solid) at room temperature. Bottom panel: L_3 -edge x-ray absorption of La in LaRu_2 (solid) and LaRu_2H_x (dots). b) Top panel: L_1 -edge x-ray absorption of Ce in the vapour state (dots) at 2500 K and in the solid state (solid) at room temperature. Middle panel: L_1 -edge x-ray absorption of Ce in CeFe_2 (solid) and CeFe_2H_x (dots). Bottom panel: L_1 -edge x-ray absorption of La in LaRu_2 (solid) and LaRu_2H_x (dots). (Adapted from refs. 1-2).

LaRu₂ before and after hydrogen charging are compared. Hydrogen destroys the long-range crystalline order with the concomitant weakening of the La(5d)-Ru(4d) hybridisation. The 5d states of La in the hydride phase are therefore more localised as confirmed from the sharper white line peak at the L₃ absorption.

3. L_{3,2} absorption and mixed valence.

In mixed valence materials macroscopic and microscopic measurements indicate the coexistence of two adjacent valence states of the lanthanide atom. We will focus in homogeneously mixed valence (*hmv*) systems (where the lanthanide atoms occupy only sites with identical point symmetry).

The focus interest in homogeneously mixed valence is the 4f electron delocalisation. In normal lanthanide solids (which have by definition integral lanthanide valence) the number of inner 4f electrons is integral, being all the 4f electrons completely localised on a given atom (i.e. there is no 4f-band formation). In a *hmv* material an electron must temporarily leave the 4f shell and after the valence transition from 4fⁿ⁺¹ to 4fⁿ it occupies one of the states of the outer 5d6s shell. If we describe the dynamics of the 4f electron delocalisation in terms of valence fluctuations, the coexistence of two valence states on a single site implies average fractional valence of each lanthanide atom, being fractional valence defined as the time-averaged ratio of the occupation probabilities of the two integral valence states. under the assumption that there are only two atomic valence configurations with finite amplitude in both the ground and excited states of the solid, such as [Xe]4fⁿ⁺¹ 5d¹ 6s² and [Xe]4fⁿ 5d²6s² .

In the case of L_{3,2}-absorption identification of the different 4f configurations involved in the mixed valent state can be only be done indirectly by identifying the corresponding two outer valence electron configuration and characteristic binding energies. As we will see in the following, the individual L_{3,2} intensities may be obtained from a straghtforwad integration procedure so that the degree of fractional valence can be extracted from the relative streghth of the two peaks appearing at the L_{3,2}-absorption edges.

Let's to consider the case of mixed valence cerium-based systems. The XANES spectra at the Ce L₃-edge shown in Fig. 16 exhibits a characteristic double peak reflecting the existence of two configurations in the initial state, 4fⁿ and 4fⁿ⁺¹ . This peculiar profile is made by the superposition of the

atomic $2p \rightarrow 5d$ transition for each ground state configuration. The white line corresponding to the $4f^{n+1}$ configuration is shifted to lower energy with respect to that of the $4f^n$ due to the screening of the additional $4f$ -electron. The detection of the two configurations in the ground state is possible because the time scale of the absorption process is two to three orders of magnitude smaller than that associated to the valence fluctuation.

Now it is possible to estimate the fractional occupation of the $4f$ configurations in the initial state, i.e., the electronic valence, starting from the intensity ratio of the two white-lines that weight the intensity in the final state^(2,3). In this way, an estimate for the Ce valence can be extracted through the deconvolution of the normalized XANES spectra by using arctangent functions to describe the transitions into the continuum states and Lorentzian functions to take account of the atomic-like $2p \rightarrow 5d$ transitions. The deconvolution process is usually performed by fitting the normalized spectra to this expression:

$$F(E) = B_0 + B_1 E + \frac{\left(\frac{\Gamma}{2}\right)^2 A_1}{(E - E_1)^2 + \left(\frac{\Gamma}{2}\right)^2} + \frac{\left(\frac{\Gamma}{2}\right)^2 A_2}{(E - E_2)^2 + \left(\frac{\Gamma}{2}\right)^2} + \frac{A_1}{A_1 + A_2} \left\{ \frac{1}{2} + \frac{1}{\pi} \right. \\ \left. \arctan \left[\frac{E - (E_1 + \delta)}{\frac{\Gamma}{2}} \right] \right\} + \left\{ 1 - \frac{A_1}{A_1 + A_2} \right\} \left\{ \frac{1}{2} + \frac{1}{\pi} \arctan \left[\frac{E - (E_2 + \delta)}{\frac{\Gamma}{2}} \right] \right\} \quad (4)$$

where E_1 and E_2 are respectively the first accessible $5d$ -states in $4f^{n+1}$ and $4f^n$ configurations; A_1 and A_2 describe the relative weight of the two configurations; Γ is the core-hole lifetime for the transition and δ is the shift between the onset of the continuum and bound-states transitions. B_0 and B_1 are the coefficients of a linear background.

4. $M_{4,5}$ and $N_{4,5}$ absorption in lanthanides.

The $L_{2,3}$ method turned out to be in general superior to all other measurements of the fractional valence being the main reasons:

i) the $L_{2,3}$ valence measurements can be performed equally on all the lanthanide atoms which show mixed valence (La, Ce, Pr, Sm, Eu, Tb, Tm and Yb),

ii) it can be at all concentrations of hmv atoms,

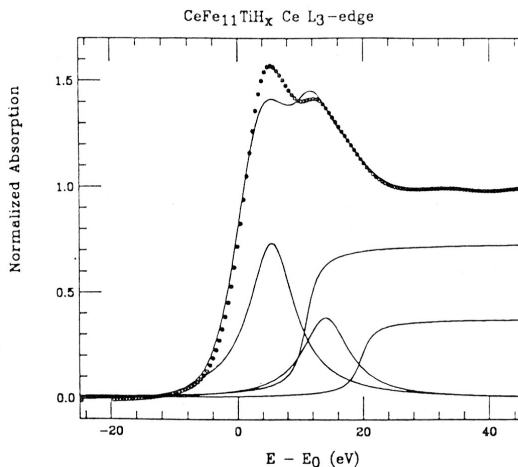


Figure 6. Deconvolution of the Ce L_3 -edge absorption spectrum in the $\text{CeFe}_{11}\text{TiH}_x$ prior (solid line) and after hydrogen uptake. The deconvolution of the Ce L_3 -edge absorption spectra shown above returns a valence of 3.33 in the case of pure $\text{CeFe}_{11}\text{Ti}$ compound that is reduced to and 3.26 after hydrogen absorption (after Ref. 4).

iii) it can be applied at all temperatures and high pressures (350 kbar),

iv) it is a bulk measurement, surface valence shifts can be neglected.

In principle this information can be also gained, even in a better way, by looking at the $M_{4,5}$ and $N_{4,5}$ absorption edges because these edges correspond to $d \rightarrow 4f$ transitions (excited core electrons belong to the 3d and 4d shell for $M_{4,5}$ and $N_{4,5}$, respectively). Therefore these $M_{4,5}$ and $N_{4,5}$ absorption edges probe directly the inner 4f configurations while those of $p \rightarrow d$ symmetry ($L_{2,3}$) probe outer electron configurations. These edges exhibit sharp final-state multiples that may serve as fingerprints of the 4f configurations, as they reproduce unambiguously the localized nature of the 4f configurations. However, analytical procedures for the extraction of the 4f occupation numbers from the two superimposed $M_{4,5}$ final-state multiplets are not so straightforward as they need detailed ab-initio calculations regarding their intensities and positions in each valence state. In addition, as absorption of $M_{4,5}$ and $N_{4,5}$ transitions are located in the soft x-ray range (800-1700 eV) and in the ultraviolet (98-205 eV), there are special experimental problems (saturation effects and surface shifts) that drastically diminish the potential of $M_{4,5}$ and $N_{4,5}$ absorption as a tool for high precision valence

determination. Notwithstanding the above remarks $M_{4,5}$ and $N_{4,5}$ absorption in the lanthanides provide also an unvaluable tool for studying 4f conduction-electron interaction as we show in the following examples.

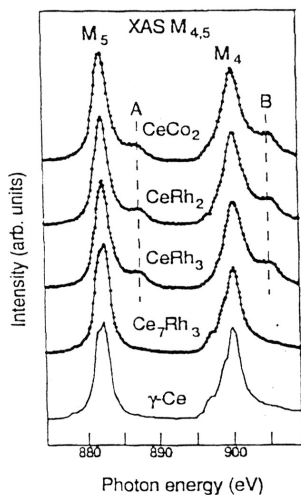


Figure 7. $M_{4,5}$ spectra of several Ce intermetallic compounds compared to that of γ -Ce (Ref. 5).

The $M_{4,5}$ spectra exhibit two main peaks which are known to be due to the $3d_{3/2}$ and $3d_{5/2}$ multiplet structure of the $3d^9 4f^2$ final state. In CeCo_2 , CeRh_2 and CeRh_3 the $M_{4,5}$ spectra show additional peaks at about 5 eV higher photon energies (labelled A and B in Fig. 7). The XAS spectra line shape of Ce_7Rh_3 is quite similar to that of γ -Ce, where only the main peaks with a clearly outlined $3d^9 4f^2$ final state multiplet structure is observed. Features A and B are interpreted as originating from $3d^9 4f^1$ final states being the energy separation of these features essentially driven by the Coulomb interaction between the 3d core hole and the 4f subshell, and by the Coulomb repulsion between the 4f electrons. Their growth is further accompanied by a shape change of the main peak arising from a washing out of the multiplet structure of the $3d^9 4f^2$ final state. These spectral shape modifications are related to the decrease of the f counts and to the increase of the hybridisation of the 4f levels with other conduction electrons.

The growth and intensity of shoulders A and B in the CeCo_2 , CeRh_2 and CeRh_3 spectra indicate a stronger interaction of the 4f electrons with the conduction states with respect to Ce_7Rh_3 and γ -Ce that, on the other hand, show a very similar degree of 4f conduction state hybridisation.

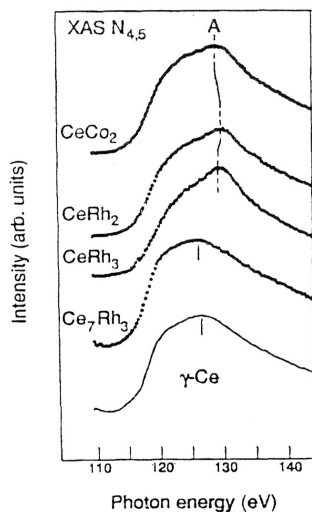


Figure 8. $N_{4,5}$ spectra of several Ce intermetallic compounds compared to that of α -Ce (Ref. 5).

The $N_{4,5}$ absorption spectra are shown for the same compounds studied above. The spectra are characterised by a broad peak corresponding to a $4d^9 4f^{n+1}$ final-state transition. The $4d^9 4f^{n+1}$ multiplet structure extends over more than 20 eV due to the strong exchange interaction caused by the large radial overlap between the 4d and 4f orbitals, being these structures strongly broadened by autoionisation into the underlying continuum, and furthermore complicated by the rather small spin-orbit splitting of the 4d hole. For these reasons, at variance with the case of $M_{4,5}$ XAS, the interpretation of the $N_{4,5}$ absorption is still controversial, and only qualitative information about the hybridisation strength could be gained.

The most striking result is that the observation of a feature at 130 eV in $CeCo_2$, $CeRh_2$ and $CeRh_3$ which is characteristic of α -Ce and of strongly hybridized Ce metallic compounds. This feature is shifted by near 5 eV to higher energies relative to the main features observed for γ -Ce and Ce_7Rh_3 ; the magnitude of this shift has been suggested to be related to the increase of the hybridisation strength.

5. Some examples for further reading.

- [1] “The influence of interstitial solutions (H, N) on the cerium electronic state in Ce-Fe intermetallic compounds: and x-ray absorption spectroscopy (XAS) study”. J. Chaboy, A. Marcelli and L. Bozukov, *J. Phys. Condens. Matter* 7, 8197 (1995).

- [2] “X-ray spectroscopic evidences of the electronic change of regime of Ce in the $CeNi_xPt_{1-x}$ solid solution”. J.I. Espeso, J.C. Gómez Sal, M.C. Sánchez and J. Chaboy, *Physica B* 259-261, 1140 (1999).
- [3] “Cerium L_3 absorption in elemental Ce and $CeCu_2Si_2$ under high pressure”. J. Röhler, in “Handbook on the Physics and Chemistry of Rare Earths”, edited by K.A. Gschneidner Jr., L. Eyring and S. Hufner, Vol. 10, (North-Holland, Amsterdam, 1987).

IV.-Magnetic Dichroism

Dichroism is the polarization dependence of the absorption in light. In general, the response of an electron charge distribution to an electromagnetic disturbance is anisotropic (directionality of chemical bonds, crystal fields, molecular orientation, etc.). Therefore, depending on the local symmetries exhibited by a material, this can lead to linear- and/or circular-polarization-dependent attenuation coefficients.

1. The basic ideas.

Magnetic dichroism is essentially an orbital phenomenon in which a photon transfers helicity ± 1 (angular momentum along the direction of the wave vector) to an absorber, exhibiting attenuation coefficients which are directly sensitive to orbital electronic polarization.

The main principle at work with magnetic dichroism is conservation of angular momentum. Within the above approach one can consider the angular momentum J' of an atom after absorbing a photon as the vector sum of the initial one J and the intrinsic spin of the photon,

$$J' = J + \sigma \quad (5)$$

where σ is the photon angular moment in the direction of propagation,

$$\sigma = \sigma \hat{q} \quad (6)$$

and σ is the photon helicity than can be +1 (right-handed circular polarization) or -1 (left-handed). Note, that the handedness of circular polarization was discussed in the precedent chapter.

2. The two-step picture

Spin dependent absorption of circularly polarized photons may be visualised as a two stage process. In this naive picture the XMCD sensitivity on the polarization of the final states stems from Fano effect⁽⁶⁾. First, a circularly polarized photon excites a photoelectron from a core level. The electron, which was initially unpolarized acquires an expectation value of its spin in photon beam direction (gains spin polarization in the interaction). In the second stage, the photoelectron is captured into an unoccupied valence state. The transition rate depends on the number of available final states with spin parallel to the photoelectron spin. Hence, differences in the spin-polarized density of states lead to different transition probabilities for spin-up and spin-down photoelectrons and, as the photoelectron spin is governed by the helicity of the absorbed photon, the transition rates become different for left- and right-handed photons.

If now we write the attenuation coefficient for $v=\pm 1$ as

$$\begin{aligned}\gamma_+(E) &= \phi[p_+(\uparrow)\rho_{\uparrow}(E) + p_+(\downarrow)\rho_{\downarrow}(E)] \\ \gamma_-(E) &= \phi[p_-(\uparrow)\rho_{\uparrow}(E) + p_-(\downarrow)\rho_{\downarrow}(E)]\end{aligned}\quad (7)$$

where $p_{\pm}(\uparrow, \downarrow)$ are the relative weights for spin-up (down) photoelectron polarization, and $\rho_{(\uparrow, \downarrow)}$ are the unoccupied densities for spin-up (down) electrons. We can calculate the fractional change in absorption by reversing either the photon helicity or the sample magnetization:

$$\frac{\Delta\gamma(E)}{\gamma(E)} = \frac{\gamma_+(E) - \gamma_-(E)}{\gamma_+(E) + \gamma_-(E)} = \left(\frac{p_{\uparrow} - p_{\downarrow}}{p_{\uparrow} + p_{\downarrow}}\right) \left(\frac{\rho_{\uparrow}(E) - \rho_{\downarrow}(E)}{\rho_{\uparrow}(E) + \rho_{\downarrow}(E)}\right) = 2P_e \frac{\rho_s(E)}{\rho(E)} \quad (8)$$

where we have introduced the charge density, $\rho(E)$, the spin-polarized density of states $\rho_s(E) = 1/2 [\rho_{\uparrow}(E) - \rho_{\downarrow}(E)]$ and the photoelectron polarization is defined to be

$$P_e = \frac{p_{-} - p_{+}}{p_{-} + p_{+}} \quad (9)$$

The value of P_e can be calculated: it is very small for K-absorption $\sim 1\%$ (since only the small spin-orbit coupling of the final p state contributes); it amounts $+1/4$ for L3 and $-1/2$ for L2 absorption⁵.

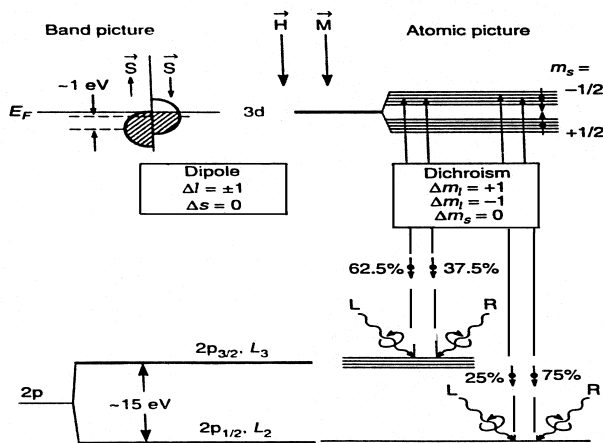


Figure 9. The two-step picture of spin-dependent absorption.

Consequently, in this simple model the spin-polarized photoelectron acts as a probe, which monitors the spin direction of the final spin-up and spin-down states, so that the normalized dichroic signal can be directly correlated to the normalized spin-density of the absorbing atom.

3. Orbital magnetization and XMCD: sum rules.

One of the most important steps for XMCD was made when Theo Thole and coworkers discovered that the integrated intensity of the XMCD signal could be related to the ground state expectation value of the orbital moment⁽⁷⁾.

The first sum rule concerns the orbital momentum. It was shown that $\langle L_z \rangle$ is proportional to the integrated intensity of the difference between the spectra taken for opposite helicities of the incoming x-rays. For an edge which is spin-orbit split the intensity for both components must be taken. The expression for the rule is

$$\rho = \frac{\int_{j_+ + j_-} d\omega (\mu^+ - \mu^-)}{\int_{j_+ + j_-} d\omega (\mu^+ - \mu^- + \mu^0)} = \frac{1}{2} \frac{l(l+1) + 2 - c(c+1)}{l(l+1)(4l+2-n)} \langle L_z \rangle \quad (10)$$

where l is the orbital quantum number of the final state, c of the core state, n is the number of electrons in the valence shell and μ_{tot}^+ , μ_{tot}^- and μ_{tot}^0 are the total (integrated over both spin-orbit split edges) absorption coefficients for a magnetic field parallel, antiparallel and perpendicular to the photon angular momentum vector.

The sum rule for the expectation value of the spin momentum is:

$$\rho = \frac{\int_{j_s} d\omega(\mu^+ - \mu^-) - [c(c+1)] \int_j d\omega(\mu^+ - \mu^-)}{\int_{j_s+j_s} d\omega(\mu^+ - \mu^- + \mu^0)} = \frac{l(l+1) - 2 - c(c+1)}{3c(4l+2-n)} \langle S_z \rangle + \frac{l(l+1)[l(l+1) + 2c(c+1) + 4] - 3(c-1)^2(c+2)^2}{6lc(l+1)(4l+2-n)} \langle T_z \rangle \quad (11)$$

Therefore, spin and orbital contributions to the local magnetic moments can be deduced directly by applying these sum-rules.

4. Selected examples

1) Local magnetic moments and magnetic coupling.

As discussed above, one of the most important capabilities of XMCD lies on the possibility of determining both local magnetic moments and the sign of the magnetic interactions.

The case of the 5d impurities (~3%, Hf, W, Re, Os, Ir, Pt, Au) in iron can be illustrative examples that the XMCD signal is in some cases directly related to the local magnetic moment of the absorbing atom.

Indeed, according to equation (8), integration of the experimental spectra yields the local d-moment (once the total density of states has been included either from theoretical calculations or from the averaged polarization-averaged absorption spectra). As shown in Fig. 28, the agreement between the moments deduced from the experimental spin-dependent absorption and the theoretical data is remarkable. In particular, the predicted change of sign of the local moment between Os and Ir, is well confirmed by the XMCD data

and, moreover, the XMCD deduced moments agree rather well to previous theoretical calculations.

Another striking capability of XMCD resides into the possibility of the direct determination of the sign of the magnetic coupling. This can be seen in Fig. 11 where the Fe K-edge and Gd L₃-edge XMCD signals of metal foils are compared to those of GdFe₂. As shown in the figure, the sign of the Fe K-edge signal is reversed, as corresponding to the antiferromagnetic coupling between the Fe and Gd sublattices in GdFe₂, being the Gd sublattice who determine the sign of the total magnetization.

2) *Element-specific magnetic hysteresis.*

The most fundamental characterization of a magnetic material is its magnetization as a function of applied field (this yields not only magnetic moment but also provides information on the magnetic anisotropy and magnetic coupling). From the hysteresis of the measurement one can extract important secondary information such as the coercive field and the remnant magnetization, which depends upon details of domain formation and reversal. Traditionally, magnetization reversal in thin ferromagnetic films has been studied via a variety of methods which includes vibrating sample magnetometry (VSM), magnetization loopers, ferromagnetic resonance, Lorentz electron microscopy, SQUID susceptometry (superconducting quantum interference device), magneto-optical Kerr effect, magnetoresistance, etc.

For magnetic systems containing more than one magnetically active element, element-specific magnetic hysteresis determination should provide novel information that is unobtainable by using conventional techniques. However, we can get this information now by means of XMCD measurements.

The first example on this capability of XMCD was provided by C.T. Chen and coworkers⁽¹¹⁾ who studied by means of XMCD the hysteresis loop of the Fe/Cu/Co trilayer system (thick Fe(102 Å)/Cu(30 Å)/Co(51 Å); thin Fe(53 Å)/Cu(30 Å)/Co(64 Å)).

By monitoring the peak-height of the XMCD signal at the L₃ edge of Fe and Co, as a function of the applied magnetic field, one obtain the curves shown in Fig. 12. The complicated conventional hysteresis curves, obtained with a VSM magnetometer, can be resolved as a linear combination of the two

elemental hysteresis curves, thereby determining the magnetic moments for the Fe and Co layers.

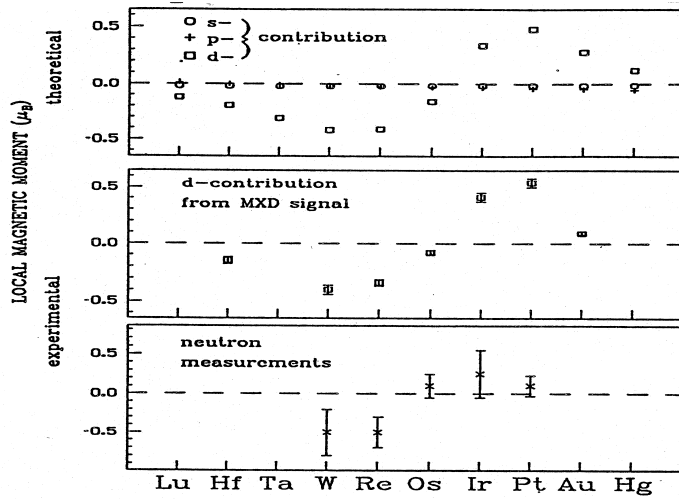


Figure 10. Calculated and experimentally deduced local magnetic moments of 5d impurities in iron (from Ref. 9).

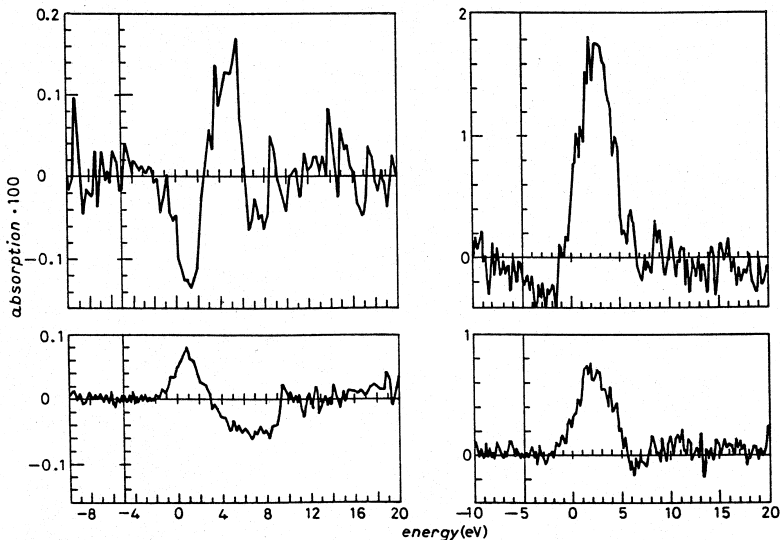


Figure 11. XMCD at the Fe K-edge in GdFe_2 (a) and in Fe metal (b). Gd L3-XMCD in GdFe_2 (c) and in Gd metal (d). Data taken from Ref. 10.

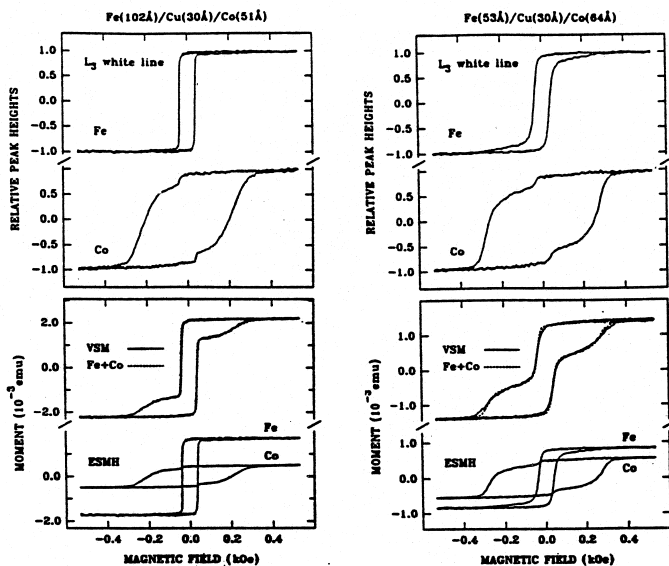


Figure 12. Top: Fe and Co XMCD L3 white-line intensities as a function of the applied magnetic field for the thick (left) and thin (right) Fe/Cu/Co trilayer samples. Bottom: macroscopic VSM-hysteresis curve and its least-squares-best-fit linear combination of the Fe and Co XMCD curves

Although the Fe hysteresis loop is representative of a single film, the fine structure observed at low field in the Co hysteresis loop clearly demonstrates that the Co film has two different components. The onset of this feature corresponds exactly with the switching of the Fe film, indicating that the Fe film and a fraction of the Co film are magnetically coupled (note that the fine hysteresis features are imperceptible in the VSM data). The fit of the VSM data to a least-square-best-fit linear combination of the Fe and Co hysteresis curves leads to values of $2.01 \pm 0.008 \mu_B$ per Fe atom and $1.2 \pm 0.05 \mu_B$ per Co atom for the thick sample, while in the case of the thin samples these values are $2.0 \pm 0.08 \mu_B$ and $1.1 \pm 0.04 \mu_B$ per Fe and Co atom, respectively. Therefore, while the moments of Fe for the two films are close to the bulk Fe moment of $2.2 \mu_B$, the Co moments (1.2 and $1.1 \mu_B$) are reduced from the bulk moment of $1.7 \mu_B$.

This work demonstrates that XMCD make element-specific magnetic hysteresis measurements now feasible and serve as a powerful means for studying heteromagnetic materials.

4. XMCD and XMLD in lanthanide materials: selected examples for further reading.

- [1] "Linear dichroism in Ce 3d X-ray absorption of CeRh₃B₂". S. Nakai, A. Kamata, K. Matsuda, H. Arai, A. Yagishita and M. Kasaya, *Physica B* 186188, 76 (1993).
- [2] "Magnetic circular dichroism in CeRh₃B₂". W. Grange, J.-P. Kappler, E. Dartyge, P. Haen, P. Lejay and A. Rogalev, *Physica B* 259-261, 1142 (1999).
- [3] "4f orbital and spin magnetism in cerium intermetallic compounds studied by XMCD". J.Ph. Schille, F. Bertran, M. Finazzi, Ch. Brouder, J.P. Kappler and G.Krill. *Phys.Rev. B*, 50, 2985 (1994).

IV.-References.

1. The attenuation of x-rays passing through matter occurs by three principal means: scattering, photoelectric absorption, and pair production. In the x-ray regime where EXAFS occurs, the photoelectric absorption dominates the attenuation process.
2. E. A. Stern and S. M. Heald, in *Handbook on the Synchrotron Radiation*, Vol. 1, Chap. 10, edited by E.E. Koch (North-Holland, Amsterdam, 1983).
3. For a complete description see for example "Handbook on the Synchrotron Radiation², edited by E.E. Koch (North-Holland, Amsterdam, 1983); "Synchrotron Radiation Research", edited by H. Winick and S. Doniach (Plenum, New York, 1981).
4. For a full discussion see for example J. Röhler, in "Handbook on the Physics and Chemistry of Rare Earths", edited by K.A. Gschneidner Jr., L. Eyring and S. Hufner, Vol. 10, (North-Holland, Amsterdam, 1987).
5. Consider for example the case of 2p absorption. Left circularly polarized light (LCP) travelling along +z gives rise to transitions with $\Delta m = +1$ ($\Delta m = -1$ for RCP). Since the electric vector acts only on the orbital parts of the electron wave-functions, this results in transitions with $\Delta m = +1$, $\Delta m = -1$ and $\Delta m = 0$. In the absence of a connection between the spin and orbital part of the electron angular momentum, both LCP and RCP

- light will excite 50% electrons with spin-up and 50% with spin down. The situation, however, changes when spin-orbit is present. Calculations show that in this case LCP excites 37.5% spin-down and 67.5% spin-up electrons at the L_3 -edge (75% and 25%, respectively, at the L_2). Dichroism (the difference of absorption for LCP and RCP light) will occur when electrons with different spins have different possibility to be absorbed into the d-band, i.e. when the d-band is exchange split.
6. G. Materlik, B. Sonntag and M. Tausch, Phys. Rev. Lett. 51, 1300 (1983).
 7. J. Chaboy, A. Marcelli and J. García, J. Magn. Magn. Mater. 166, 149 (1997).
 8. J. Röhler, J. Magn. Mag. Mat. 47-48,175 (1985).
 9. J. Chaboy, A. Marcelli , L. Bozukov, F. Baudelet, E. Dartyge, A. Fontaine and S. Pizzini, Phys. Rev. B 51, 9005 (1995).
 10. P. Vavassori, L. Duó, G. Chiaia, M. Qvarford and Y. Lindau, Phys. Rev. B 52, 16503 (1997).
 11. U. Fano, Phys. Rev. 178, 131 (1969)
 12. B.T. Thole, P. Carra, F. Stte and G. van der Laan, Phys. Rev. Lett. 68, 1943 (1992); P. Carra, B.T. Thole, M. Altarelli and X. Wang, Phys. Rev. Lett. 70, 694 (1993)
 13. C.T. Chen, Y. U. Izerda, H.-J. Lin, N.V. Smith, G. Meigs, E. Chaban, G.H. Ho, E. Pellegrin and F. Sette, Phys. Rev. Lett. 75, 152 (1995)
 14. G. Schütz, R. Wienke, W. Wilhelm, W. Wagner, P. Kienle and R. Frahm, Z. Phys. B75, 495 (1988); H. Ebert, B. Dittler, R. Zeller and G. Sol. State Commun. 69, 485 (1989)
 15. F. Baudelet, C. Brouder, E. Dartyge, A. Fontaine, J.P. Kappler and G. Krill, Europhys. Lett. 13, 751 (1990).
 16. C.T. Chen, y.U. Idzerda, H.-J. Lin, G. Meigs, A. Chaiken, G.A. Prinz and G.H. Ho, Phys. Rev. B 48, 642 (1993).